MULTIDECADAL CLIMATE VARIABILITY IN OBSERVED AND SIMULATED SURFACE AIR TEMPERATURE AND SEA-LEVEL PRESSURE

by

Andrew Westgate

A Thesis Submitted in

Partial Fulfillment of the

Requirements for the Degree of

Master of Science

in Atmospheric Science

at

The University of Wisconsin-Milwaukee

May 2020

ABSTRACT

MULTIDECADAL CLIMATE VARIABILITY IN OBSERVED AND SIMULATED SURFACE AIR TEMPERATURE AND SEA-LEVEL PRESSURE

by

Andrew Westgate

The University of Wisconsin-Milwaukee, 2020
Under the Supervision of Professor Sergey Kravtsov

Accurate estimates of multidecadal climate variability generated internally within the climate system are required to gauge anthropogenic contribution to warming trends and to develop efficient strategies to mitigate climate change. Previous analyses of historical surface air temperatures (SAT) showed that numerical climate prediction models lack a pronounced global mode of observed internal variability — the stadium wave (SW), — which represents a multidecadal undulation originating in the North Atlantic and propagating to other regions of the globe. The present study extends these analyses by exploring co-variability of SAT and sea-level pressure (SLP) within the SW. Addition of SLP data does not substantially affect the SAT component of SW, which is essentially identical to its SAT-only counterpart. The SW's SLP features point to atmospheric teleconnections and dynamical mechanisms behind its global propagation. Finally, the climate model analogs of SW exhibit quasi-stationary, often smaller-scale patterns relative to observations, and lack of global propagation.

TABLE OF CONTENTS

LIST OF FIGURES

ACKNOWLEDGEMENTS

Thank you to Dr. Kravtsov for providing the instruction needed to complete this project. Not only was he receptive to questions but also guided me through many concepts I had not had exposure to during my undergraduate studies.

Thank you to Dr. Evans and Dr. Roebber for serving on my committee alongside Dr. Kravtsov.

Lastly, thank you to my family and friends who provided support in regard to this project and beyond.

1. Introduction

Understanding the observed decadal climate variability (DCV) is vital to gaining a better understanding of the earth's climate system as a whole. With anthropogenic influences on climate, and the drastic increases in greenhouse gas concentrations and long-term global temperature, more significance is placed on this understanding (Cassou et al. 2018). Embedded within this increase in global temperature are "hiatuses" where the global temperature increase exhibits a slope of around 0 for roughly two decades (Lewandowsky et al. 2016; Barcikowska et al. 2017). In fact, it was the most recent hiatus that brought attention to the discrepancy between observations and climate models (Barcikowska et al. 2017; Kosaka and Xie 2013; England et al. 2014).

The key issue with DCV is the large number of processes that contribute to its phases and signals. For example, it is understood that the Atlantic meridional overturning circulation (AMOC) heavily contributes to the Atlantic Multidecadal Variability (AMV, equivalent to Atlantic Multidecadal Oscillation), as well as several other climate modes, such as the Pacific Decadal Variability (PDV) (Zhang et al. 2019). Studies have speculated from observations that PDV lags behind AMV by approximately 10 years (Chylek et al. 2014; d'Orgeville and Peltier 2007). It has been shown, through both observations and a simulation, that a positive phase in AMV is connected to warming over the western tropical Pacific and North Pacific via teleconnections (Barcikowska et al. 2017). It was also shown that this multidecadal mode is linked to AMOC (Barcikowska et al. 2017; Yeager and Robson 2017). Essentially, despite these oceanic basins being largely separated by land masses, all are connected through atmospheric circulations (Cai et al. 2019; McGregor et al. 2014; Li et al. 2016)

Another key observation is the anticorrelated eastern Pacific in regard to the North Atlantic (Barcikowska et al. 2017). Much like the AMV, multidecadal modes in the Pacific are known to be present but the characteristics and causes are still open for interpretation (Mestas-Nunez and Miller 2006; Newman et al. 2016). Mestas-Nunez and Miller (2006) speculated that the eastern Pacific shows little evidence of multidecadal variability, although this conclusion is subject to a large amount of uncertainty intrinsic to methodologies associated with detection of multidecadal climate signals. Therefore, advanced statistical methods are key when attempting to isolate multidecadal signals in the background of unpredictable climate noise.

The complex nature of the observed climate systems mentioned above, and all of its unknowns, are complicated further by imperfect climate models. While the understanding of observed DCV is limited by a short climate record and limited observations in some regions (Deser and Phillips 2017), models tend to lack the ability to replicate many features that contribute to multidecadal modes (Meehl et al. 2014). Climate prediction efforts are coordinated via the Coupled Model Intercomparison Project (CMIP). Phase 5 of this project (CMIP5: Taylor et al. 2012) is a collection of models used to predict future climate. However, it also includes historical runs, as well as runs that replicate past climates referred to as preindustrial control runs. Historical runs include external forcing factors that occur both naturally, such as volcanic eruptions and solar events, and anthropogenic forces, such as aerosols and greenhouse gas emissions through the combustion of fossil fuels. The control runs also include external forcing, but these are held constant at preindustrial levels. Multiple historical realizations (an ensemble of simulations) are typically available for each model; these realizations are obtained by initializing the model from independent states taken from pre-industrial control runs and running the historical simulation under the identical variable forcing. In this study, we used ensembles of

historical runs to infer both the internal variability and forced signal components of climate variability; the latter component includes the anthropogenic influence. The key element of this procedure (see, for example, Kravtsov and Callicutt 2017) invokes taking an ensemble average of historical simulations to estimate the forced signal, which tends to remove internal variability uncorrelated in the independent realizations of historical climate change (see section 2 for details).

Kravtsov (2017) and Kravtsov et al. (2018) showed, among other studies, that CMIP5 models underestimate the magnitude of internal multidecadal internal variability in surface air temperature (SAT), leaving the forced signal as a dominant component of the CMIP5 simulated 20^{th} century climate change. Kravtsov et al. (2018) used advanced spatiotemporal filtering methods to highlight the disparities between observed and simulated internal variability in SAT. These authors formed the differences between filtered SAT signals based on observations and individual CMIP5 simulations (optimally rescaled to reflect the observed climate sensitivity) to estimate the observed internal variability. The differences between the individual simulations of each model with respect to this model's ensemble-mean SAT time series served as estimates of the internal variability in CMIP5 models. Via multidecadal signal detection methodology, the authors showed that not only do the models contain a significantly smaller amount of internal variability than observations, but that the dominant space–time features of observed multidecadal variability are not present in the model simulations (see section 3). In particular, the dominant multidecadal signal in observations is characterized by the global oscillation-like mode termed the stadium wave (SW; Wyatt et al. 2012), which originates in the North Atlantic and propagates into other oceanic basins through atmospheric teleconnections, 'moving' into the North Pacific,

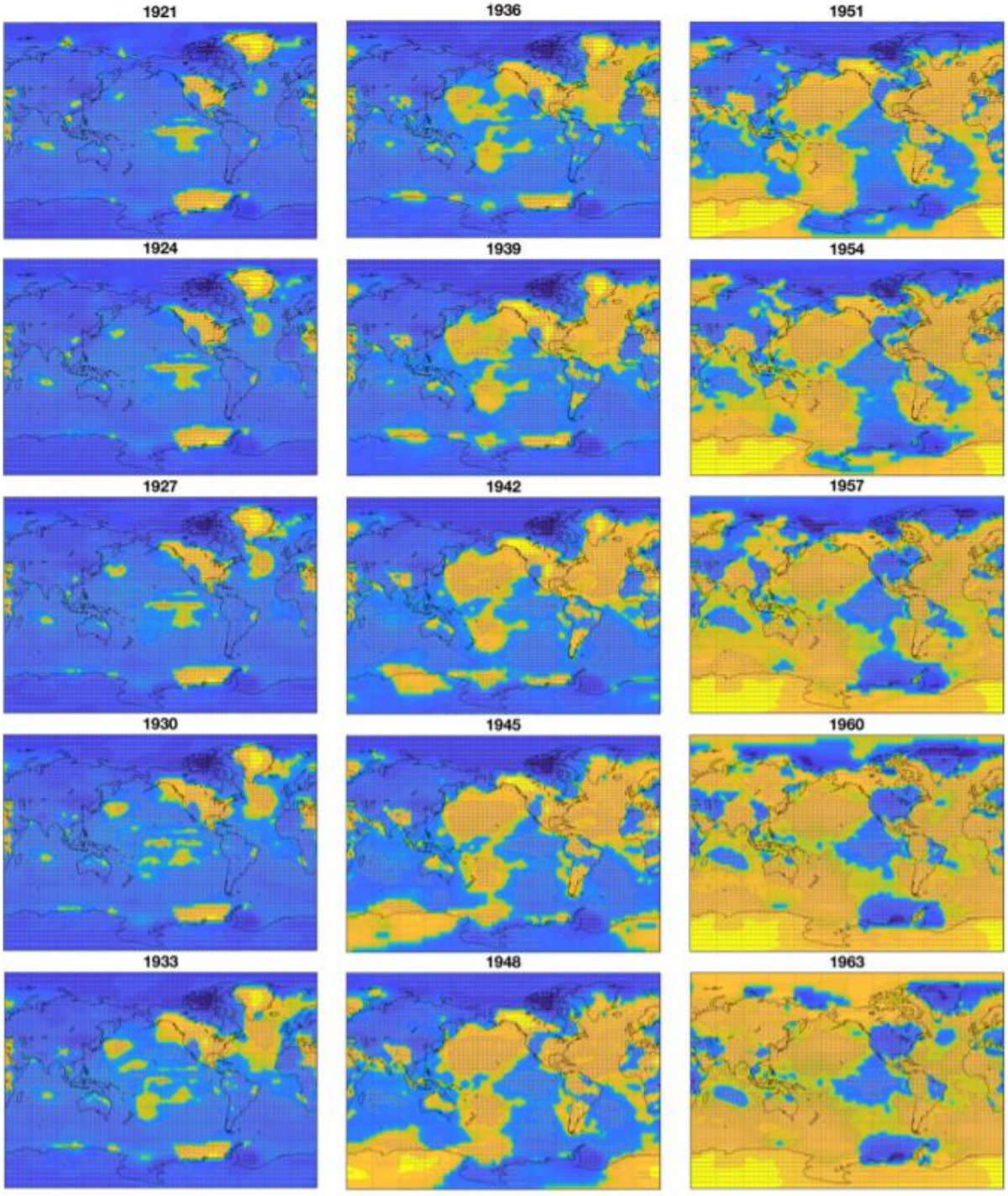

Figure 1: Kravtsov et al. (2018) Figure 4, SAT-only RC SW: Spatial plot showing the propagation of observed stadium wave with origins in the North Atlantic present in observed reconstructed SAT data. Stippling indicates statistically significant points. Positive values are warm colors and negative values are cool colors.

followed by the southwest Pacific, Antarctica, South Atlantic, and lastly the Arctic, upon which the opposite phase of the oscillation begins (**Fig. 1**).

In an effort to visualize and analyze the atmospheric teleconnections linking the features found in SAT-based SW, this study extends the analysis in Kravtsov et al. (2018) to include, in addition to SAT, observed and simulated sea level pressure (SLP) data. Instead of optimal filtering employed in Kravtsov et al. (2018), we use here a simpler method based on regional averaging to filter out some of the higher-frequency noise and thus increase signal-to-noise ratio, while obtaining essentially identical to SAT-only SW results. In conjunction with adding SLP data, we seek to 1) replicate the SAT structure of SW features found using the SAT-only analysis; 2) analyze key SLP features that highlight particular teleconnections that could cause the propagation of the SW; and 3) compare, in detail, the simulated SAT–SLP data to observations.

2. Data and methods

In lieu of climate 'observations,' we used annual surface air temperature (SAT) and sea level pressure (SLP) data (1880–2005) based on the National Oceanic and Atmospheric Administration (NOAA) Twentieth Century Reanalysis (20CR) dataset (Compo et al. 2011), version 2c. We also used annual SAT and SLP model data over the same time period from the ensemble of 111 historical simulations within the CMIP5 ensemble (Taylor et al. 2012), provided by the World Climate Research Program (WCRP) Working Group on Coupled Modeling (WGCM). These simulations came from a total of 17 different climate models and are the same simulations analyzed in Kravtsov and Callicutt (2017), Kravtsov (2017) and Kravtsov et al. (2018). All of these data were interpolated to a 2° uniform grid covering the globe prior to further analysis.

We first formed anomalies by subtracting, from each field, its 1880–2005 climatology. The forced signals in the 17 individual-model ensembles were estimated as the ensemble-mean SAT or SLP smoothed by an 11-yr boxcar running average filter (Kravtsov and Callicutt 2017); subtracting these forced signals from individual simulations of the corresponding model results in 111 estimates of the internal variability in CMIP5 simulations. The 17 forced-signal estimates above (whose spread encompasses model uncertainty) were also used as estimates of the forced signal to be used in conjunction with observation. To do so, however, we rescaled these signals using linear regression, to best match the observed time series at each grid point. Subtracting the 17 rescaled forced signals from observed time series at each grid point gives 17 estimates of the observed internal variability.

The SAT and SLP data at each grid point are heavily contaminated by smaller-scale noise and have a low signal-to-noise ratio with respect to multidecadal variability, making it difficult

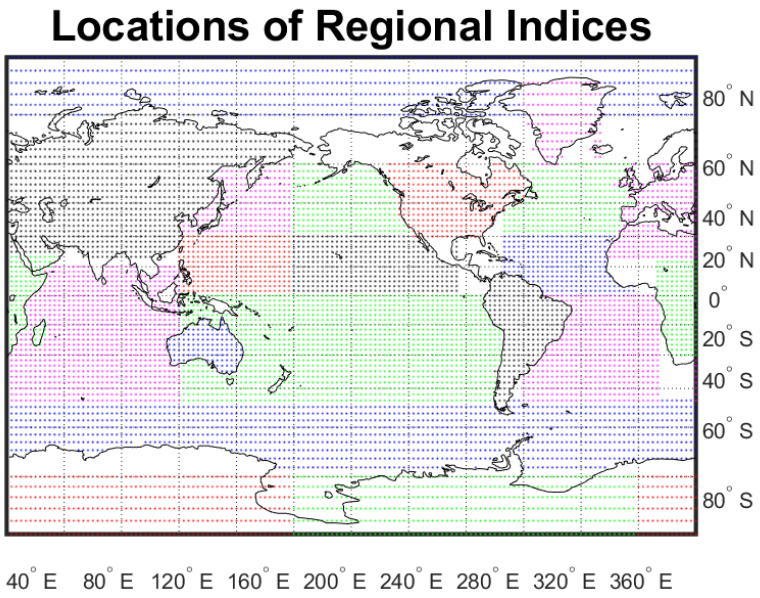

Figure 2: Resulting regional indices based on SAT and SLP PCA

to discern the signal. To reduce noise and increase the signal-to-noise ratio, we worked with, instead of the data at grid-point level, the regional averages of SAT and SLP data over 20 regions subjectively chosen to represent centers of action found in the SAT and SLP internal variability (**Fig. 2**). This method (similar to the one used in Kravtsov and Spannagle 2008) is much simpler than a fairly involved spatiotemporal optimal filtering method used in Kravtsov et al. (2018) but turns out to produce essentially identical results with respect to the SAT-only SW (section 3).

Fig. 3 shows 17 (CMIP5-based) estimates of the forced signal in observed SAT and SLP data (smoothed rescaled SMEM) with superimposed raw annual SAT and SLP data from the North Atlantic and North Pacific (obtained by averaging over two original boxes within the North Atlantic and four original boxes within the North Pacific region in Fig. 2). The difference between the 17 estimates and the raw observations represent our 17 estimates of the internal climate variability in observations. These plots visually represent the long-term trend and the uncertainty of the forced signal (and hence, also, the uncertainty of internal variability) in a given

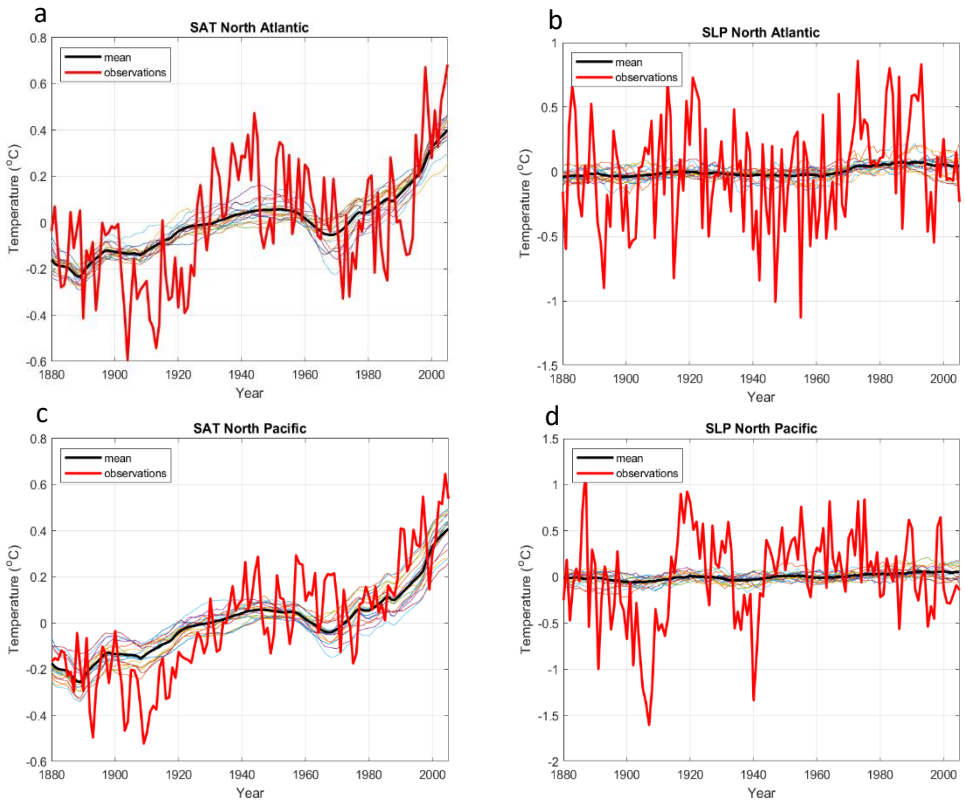

*Figure 3: Decomposition of the observed variability into forced and internal components. Time series of 17 CMIP5-based estimates of the observed forced signal (thin colored lines), the ensemble mean of the forced signal over these estimates (heavy black line), and raw observations (heavy red line) for: (**a**) SAT in the North Atlantic; (**b**) SAT in the North Pacific; (**c**) SLP in the North Atlantic; and (**d**) North Pacific (bottom right).*

region. Note the pronounced multidecadal deviations of raw observations from the estimated forced signals visually apparent in each figure panel. In SAT field, these are regional manifestations of the global SW found in Kravtsov et al. (2018). Interestingly, such deviations are also present in the SLP data (for example, in Fig. 3b for the North Atlantic region), suggesting a substantial reflection of SW in the SLP fields as well. Characterizing the SLP branch of the SW is the main focus of this thesis.

To identify the dominant multidecadal signals in our multivariate regional data, we use classical signal detection methods. Principal Component analysis (PCA), also known as Empirical Orthogonal Function (EOF) analysis (Wilks 2011), finds linear combinations of

original multi-variate time series (in our case regionally averaged SAT or SLP data) with spatial weights (EOF patterns) that maximize the variance of the resulting weighted time series (principal components, PCs). The leading EOF corresponds to the PC with largest variance, the second EOF/PC pair has second largest variance and so forth. These variances are typically presented together in the EOF variance 'spectrum' plot and are usually expressed in units of a fraction of the total variance. The EOFs can be found as eigenfunctions of the original data's covariance matrix, with the corresponding eigenvalues equal to the variance of their PCs. The sum of all EOF modes reconstructs the original data exactly, but, typically a limited number of EOFs and PCs is sufficient to describe most of the variability in the data set; hence, EOFs are most frequently used for data compression.

M-SSA (Ghil et al. 2002) is an EOF analysis applied to an extended set of the original data and lagged copies thereof. This adds an additional (temporal) dimension to the original EOF analysis that allows for the detection of structures in both space and time; M-SSA can transcend an EOF analysis in the sense that a single M-SSA mode can capture variability of several EOF modes. The EOF 'patterns' from M-SSA analysis are referred to space–time EOFs (ST-EOFs) and its PCs as space–time PCs (ST-PCs). The variability associated with a single M-SSA mode or a sum of M-SSA modes can be reconstructed in the original physical space and visualized in the same way as the original data (observed throughout time as a progression of spatial maps). These reconstructions are referred to as Reconstructed Components (RCs) and represent, in effect, an objectively filtered versions of the original multivariate input time series. The M-SSA modes can be succinctly characterized by their variance spectrum, which is analogous to the variance spectrum of the ordinary EOF analysis.

To utilize M-SSA, we first computed combined (or common) SAT/SLP EOFs of a given observed or simulated realization being considered. To do so, we started with computing the individual-field EOFs based on our 20 regional time series weighted by the size of the corresponding region to achieve area-weighted contributions from each region to the global-mean variance. The resulting 20 PCs for each field were normalized by the standard deviation of the corresponding PC-1, concatenated and decomposed into its own EOF modes and PCs (common EOFs and PCs). The physical-space patterns associated with each common EOF were obtained by regressing the original fields *on the original grid* onto the common PCs, which allowed us to visualize the climate variability over the globe at a grid point level despite the EOF (and M-SSA) analysis were performed using a limited number of regional time series. All 40 common PCs were then used as inputs to M-SSA with the maximum lag (also known as embedding dimension) M=65 (yr), chosen to maximize the separation between the leading and trailing M-SSA modes in observations (Kravtsov et al. 2018). We visualized M-SSA results by plotting M-SSA variance spectra and RCs associated with the leading pair of M-SSA modes [which, in observations, represents the Kravtsov et al.'s (2018) SW].

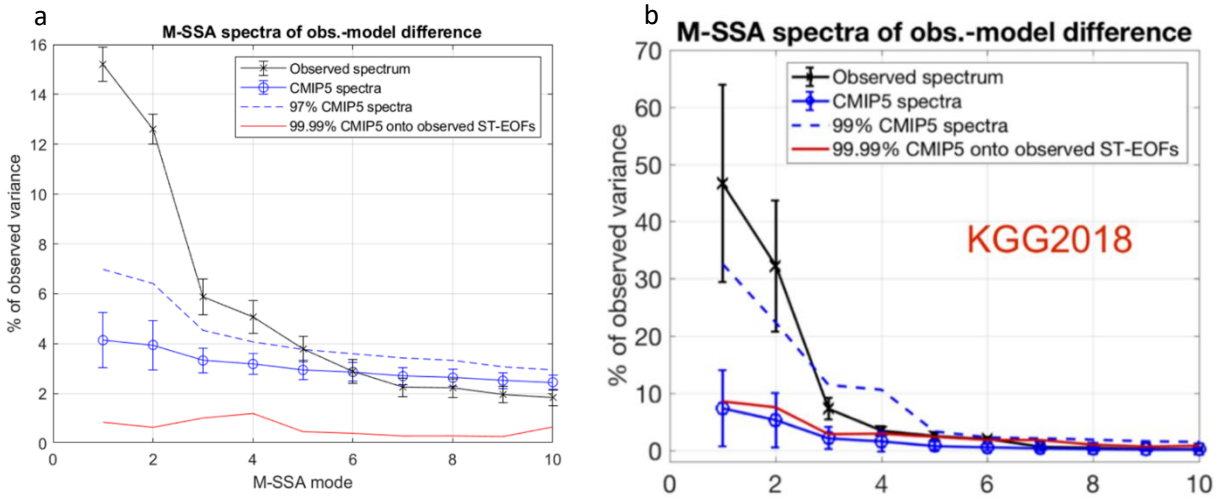

Figure 4: M-SSA variance spectra visualizing the difference in internal variability between models and observations. Spectra based on observations are in black, the CMIP5 spectra are in blue, with the error bar showing the 95% spread around the ensemble-mean values in each case; the 97th percentile of the CMIP5 ensemble mean (dashed blue), and the 99.99th percentile of the CMIP5 data projected onto the observed ST-EOFs (red). ***(a)*** *The present SAT/SLP analysis;* ***(b)*** *SAT-only analysis (Kravtsov et al. 2018).*

3. Results

3.1 Replicating the results of SAT-only Analysis

Fig. 4 shows observed and simulated M-SSA spectra based on the present SAT/SLP analysis and Kravtsov et al. (2018) SAT-only analysis. In both studies, observations have a majority of their variance contained within the first pair of M-SSA modes, whereas the M-SSA spectrum is much flatter in the models. Also, the stark difference in variance between the reanalysis and CMIP5 data shows that estimated observed internal variability is much higher than simulated internal variability. Lastly, the variance associated with projection of CMIP5 model data onto the leading ST-EOFs of reanalysis is negligibly small (the 99th percentile of these variance is shown in Fig. 4). This signifies the absence, in the models, of space-time structures replicating the observed multidecadal variability.

In the combined SAT–SLP plot, the total variance percentage is lower than that in Kravtsov et al. (2018). This is due to their filtering methodology removing more of the high frequency variability than the regional analysis, leaving the low-frequency SW to account for a larger fraction of the remaining low-frequency variability. A second distinction is the error bars (that is, the spread of variances between individual estimates of the observed or CMIP5 simulated internal variability) being much smaller in the combined SAT–SLP analysis compared to SAT-only case. This is the result of PC normalization in the combined SAT analysis, which removes some of the variance associated with the uncertainty in the intensity of the leading PC across the individual realization, leading to a smaller spread of M-SSA modal variances. Indeed, our SAT-only analysis of regional averages (not shown) replicates the SAT/SLP M-SSA ensemble-mean variance spectrum in Fig. 4a but indicates a larger uncertainty of M-SSA modal variances consistent with Kravtsov et al. (2018); Fig. 4b. Hence, the M-SSA variances based on

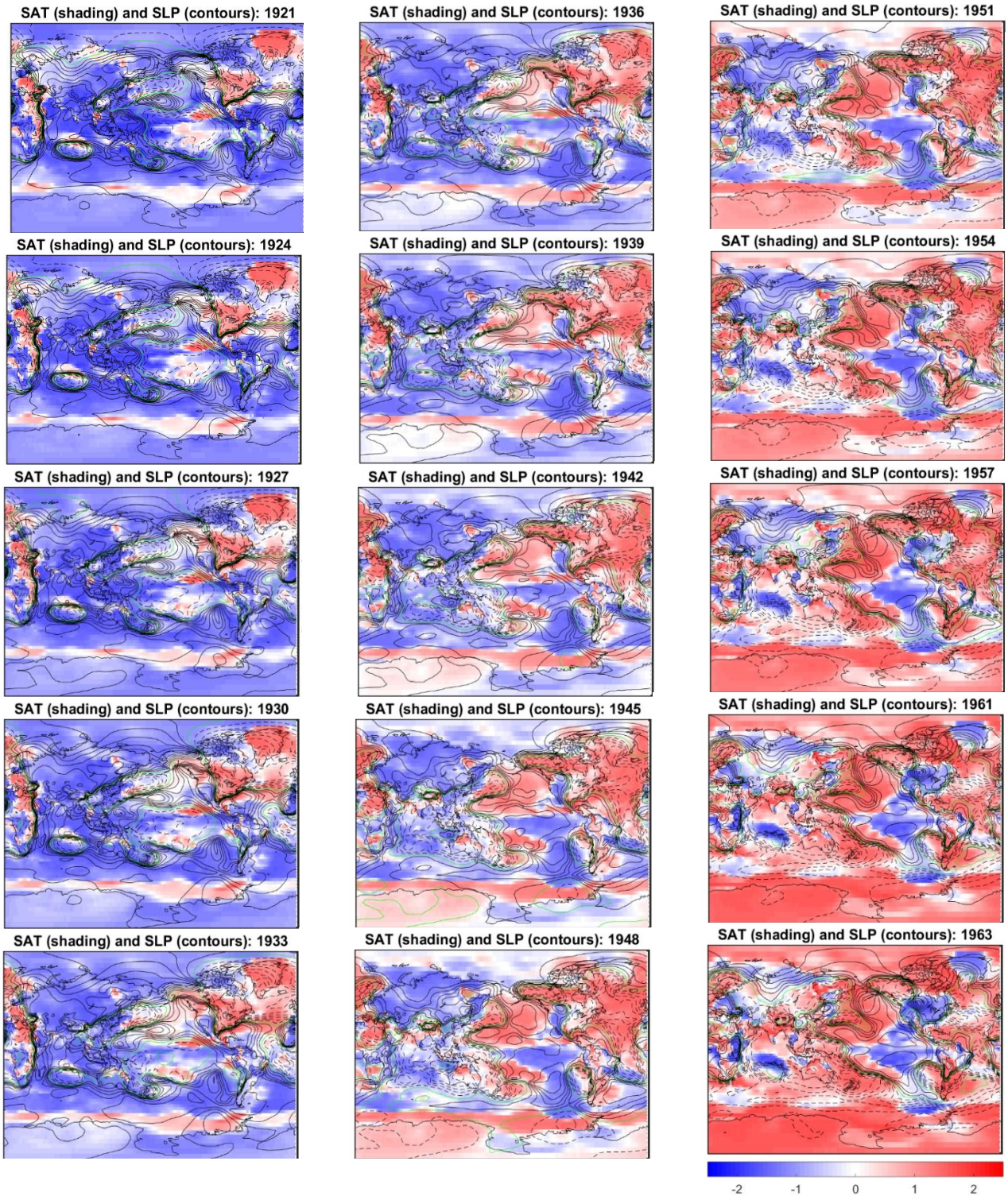

Figure 5: Observed SAT/SLP RC SW: Spatial plot showing the propagation of observed stadium wave with origins in the North Atlantic present in observed reconstructed SAT (shaded) and SLP (contours) data. Positive SLP data are denoted by solid black contours, negative by dashed contours, and 0 by green contours. Contours are spaced by 0.25. Stippling indicates statistically significant points. Positive values are warm colors and negative values are cool colors.

the combined SAT/SLP analysis do not reflect the actual magnitudes of M-SSA modes due to normalization, but assess, instead, the shape of the M-SSA variance spectrum (flatter in models, more peaked, with the dominant leading pair, in reanalysis). A way to bring in the actual magnitude of M-SSA modes to the M-SSA variance plot would be to normalize the SAT and SLP PCs in each model simulation by the standard deviation of the leading PC of the ensemble-mean observed internal variability, rather than by the standard deviations of their own PC-1.

The SAT evolution associated with the leading M-SSA pair of the reanalysis data (**Fig. 5**, shading) show the same SW feature as in Kravtsov et al. (2018) (compare with Fig. 1 here). A positive phase of the SW in SAT anomalies originates in the North Atlantic around 1921 and continues to expand. This eventually moves into the North Pacific basin, followed by the southwest Pacific, Antarctic, South Atlantic, and Arctic regions.

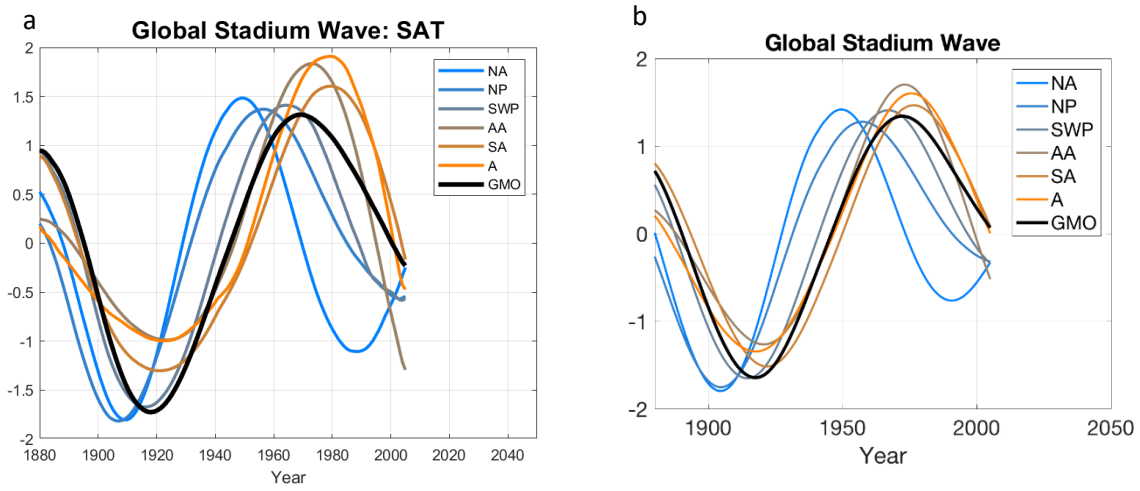

*Figure 6: Regional Indices time series of observed RC SAT data for North Atlantic (NA), North Pacific (NP), southwest Pacific (SWP), Antarctic (AA), South Atlantic (SA), Arctic (A), and the global mean (GMO). (**a**) SAT-SLP combined analysis and (**b**) SAT-only analysis (Kravtsov et al. 2018).*

The SW propagation apparent in the RC 2-D graphs can also be visualized by plotting the regional time series, which exhibit identical structure in the present analysis and that of Kravtsov et al. (2018) (compare **Figs. 6a** and **6b**), perhaps with a very slight differences in the relative amplitudes of the SW regional indices.

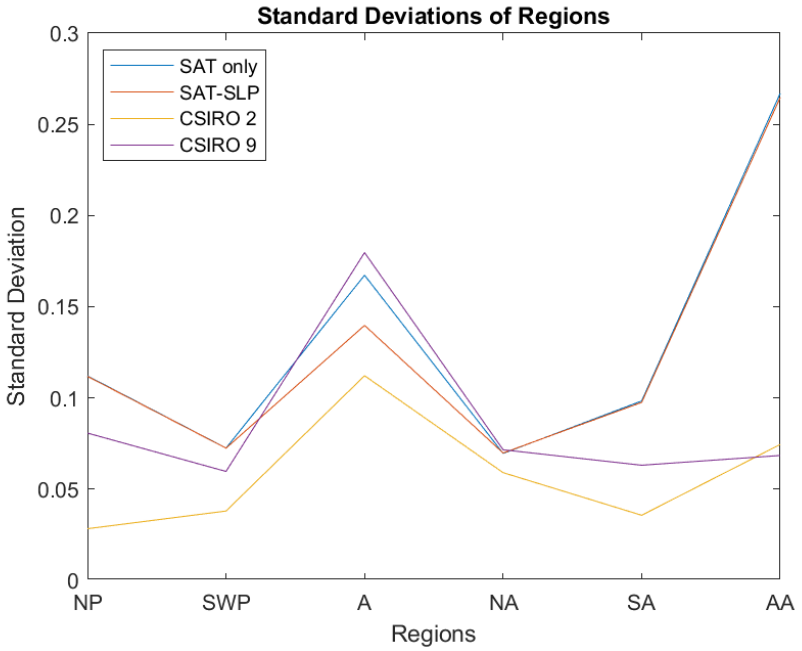

Figure 7: Dimensional standard deviations of the SW, standard deviations of SAT reconstructed data for the SAT-only analysis observations (blue line), SAT-SLP analysis observations (red line), CSIRO run 2 (yellow line), and CSIRO run 9 (purple line) for selected regions (see Figure 6 caption).

It is important to note that the patterns shown in Fig. 5 (and all subsequent spatial plots) and the time series in Fig. 6 have normalized data and do not show the magnitude of SAT anomalies, only spatial patterns or standardized regional indices. The dimensional standard deviations of the SW regional indices (**Fig. 7**) indicate the value of around 0.1ºC for ocean indices and higher standard deviations of 0.2–0.3ºC for the Arctic and Antarctic regions. The SW magnitudes based on SAT-only and SAT–SLP analysis of observations (reanalysis data) are virtually identical in all regions (with some small differences in the Arctic).

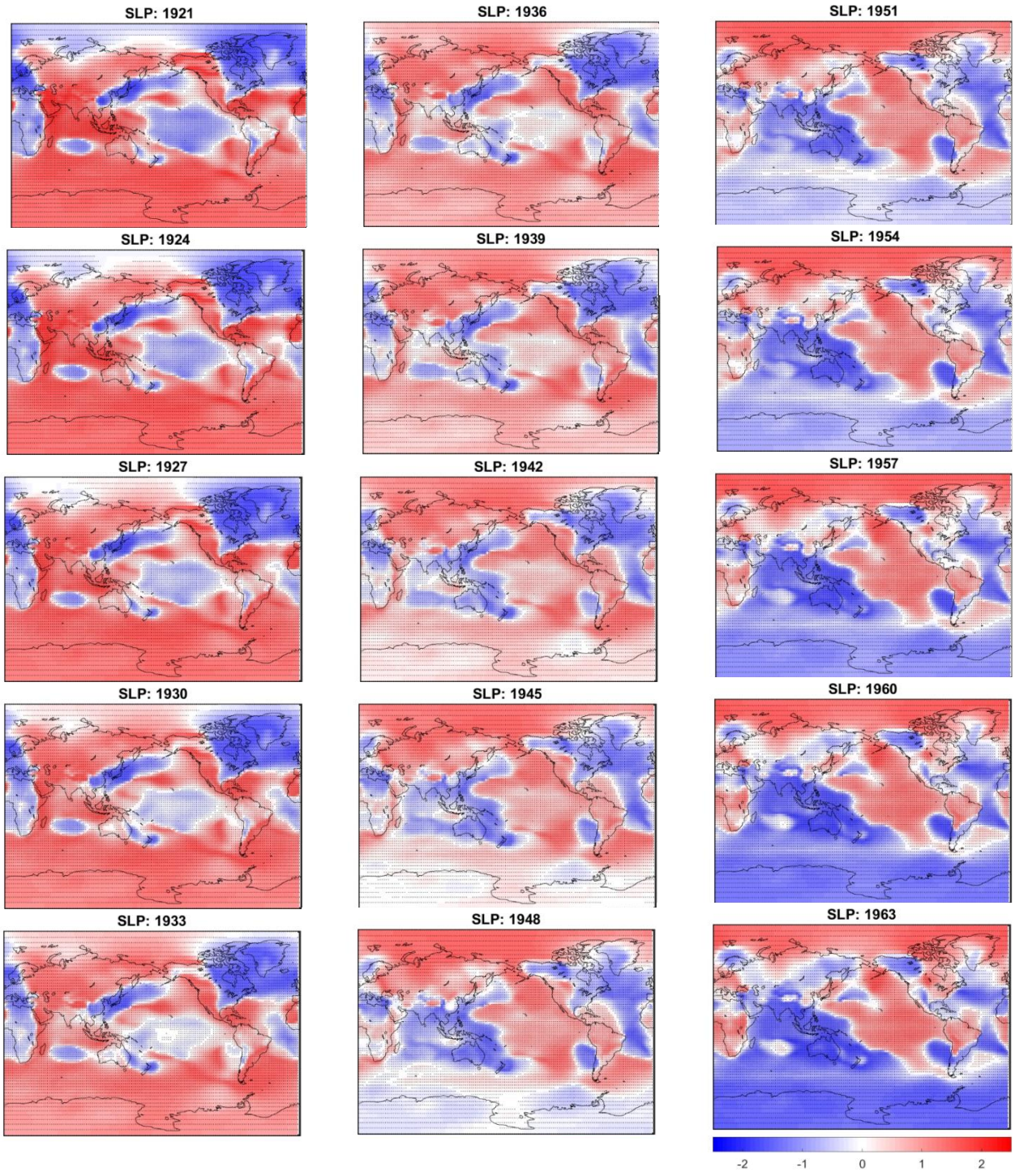

Figure 8: Observed SAT/SLP RC SW: Spatial plot showing the propagation of observed stadium wave with origins in the North Atlantic present in observed RC SLP. Stippling indicates statistically significant points. Positive values are warm colors and negative values are cool colors.

Overall, despite the addition of SLP data, which used an alternative filter through regional averaging and required the utilization of common EOF analysis to pre-process M-SSA input data, the present analysis successfully reproduces the SAT component of the observed stadium wave found in Kravtsov et al. (2018).

3.2 SLP component of the Stadium Wave

In addition to replicating the SAT-only spatial plots and time series, the inclusion of SLP data allows for an atmospheric (SLP) component of the observed stadium wave to be analyzed (**Fig. 8**). We discuss the progression of SLP anomalies within the stadium wave starting, arbitrarily, with the phase at which the global SAT associated with the SW is minimum (Figs. 1, 5 and 6), which happens around year 1920. At this time, global-scale high-pressure anomaly prevalent south of 40ºS also extends well into the Southern Hemisphere over the Atlantic and Indian Ocean sectors, accompanied by near-neutral (slightly negative) SLP anomalies in the tropical Pacific and North Pacific high — Aleutian low type of dipole in the North Pacific. The SLP pattern over the North Atlantic is also dipolar, reminiscent of the positive phase of the North Atlantic Oscillation (NAO), with negative SLP anomalies over the Arctic and positive SLP anomalies over the tropical Atlantic; the latter positive anomalies signify a large-scale east–west pressure gradient between tropical Atlantic and tropical Pacific. By 1930, all these features still prevail, but keep losing their intensity, further leading to structural changes in the regional SLP anomalies which appears to be initiated from the tropics. In particular, the SLP gradient between the tropical Atlantic and Pacific flattens out at 1930 and flips sign shortly thereafter, with the lobes of east-west oriented tropical SLP Atlantic/Pacific dipole merging with the remnants of the northern lobe of the NAO and an expanding North Pacific high, respectively, thereby leading to basin-wide positive SLP anomalies over most of the Pacific Ocean (with the exception of

negative SLP anomalies along its western coastal boundary) and negative SLP anomalies over most of the Atlantic Ocean (except for positive SLP anomalies between 20º and 60ºS) by 1940. At the same time, the positive SLP anomalies over northern Eurasia progress into the Arctic, while the Indian Ocean SLP anomalies decay to near-zero values. Further evolution of the SLP component of SW mainly involves intensification and expansion of negative SLP anomalies over Southeastern Pacific and the Indian ocean to the entirety of the region south of 40ºS, as well as the development of dipolar features in the North Atlantic and Pacific Oceans representing, roughly, the negative SW phase by year 1963 (compare with 1921 panel of Fig. 8).

The superimposed SLP contours allows for a direct comparison to the features in the SAT data (Fig. 5). Many areas around the globe exhibit SLP phases that are opposite of the SAT data, indicating that warming phases are coupled with lower SLP and cooling phases with higher SLP. This indicates that either 1) warmer SATs force SLP to fall or 2) low SLP brings conditions, such as clouds and precipitation, that forces SAT. This behavior does not appear to be unique to oceans as patterns are not consistently defined by land and ocean regions, but rather transcend over both land and water. This is not the case in the Northern Pacific and Arctic regions, however, where a large portion of each region appears to be in the same phase (positive or negative) as the SAT anomalies. Regions with persistent SAT structures, such as the central Indian ocean, have persistent SLP features as well. The SLP phases in the Indian Ocean lag the SAT phases. The dipoles mentioned in the previous paragraph appear to be co-located with smaller SAT features over Greenland – North Atlantic and Japan – northwest Pacific.

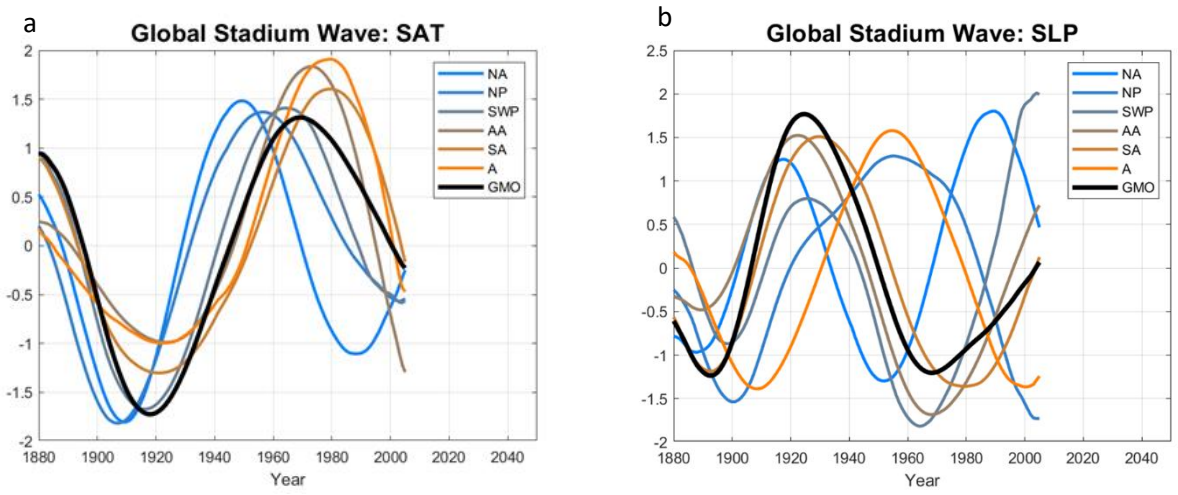

*Figure 9: Regional Indices time series of observed RC SAT data for North Atlantic (NA), North Pacific (NP), southwest Pacific (SWP), Antarctic (AA), South Atlantic (SA), Arctic (A), and the global mean (GMO).**(a)** SAT component of SAT-SLP combined analysis and **(b)** SLP component of SAT-SLP combined analysis*

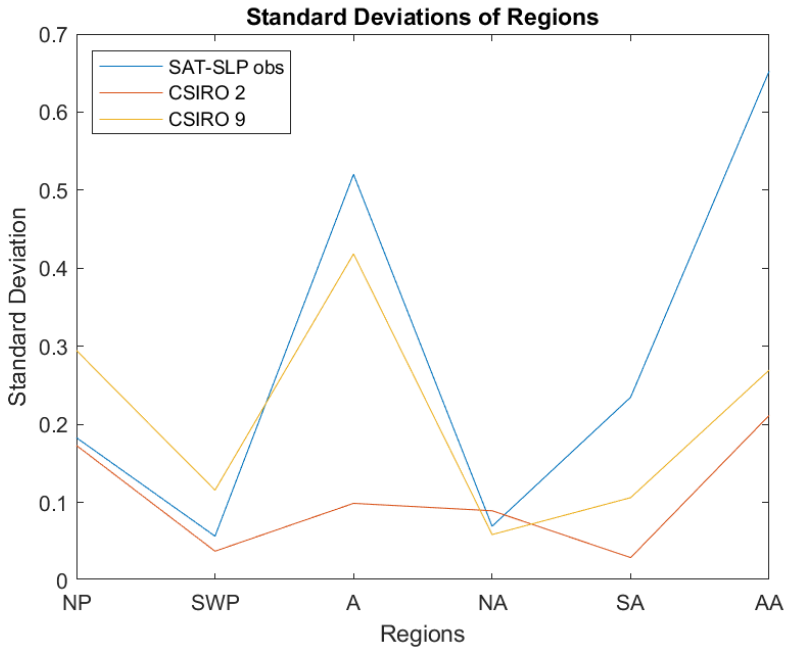

Figure 10: Dimensional standard deviations of the SW, standard deviations of SAT reconstructed data for the SAT-SLP analysis observations (blue line), CSIRO run 2 (red line), and CSIRO run 9 (yellow line) for selected regions (see Figure 6 caption).

The normalized, area averaged reconstructed SAT data (**Fig. 9a**) were compared to the area averaged reconstructed SLP data (**Fig. 9b**) utilizing the same regional indices as in Figure 6. These emphasize the features present in the spatial plots; all regions exhibit opposite phases from the SAT time series, with the exception of the North Pacific and the Arctic regions. Further, for the regions that exhibit an opposite SLP phase from the SAT SW, peaks in phases occur at the same time as peaks in the SAT SW.

Standardized regional indices for SLP are shown in **Fig. 10**. Magnitudes over ocean indices range between approximately 0.1 and 0.2, with the Arctic and Antarctic regions being around 0.5 and 0.6, respectively. SLP magnitudes exhibit higher values over polar regions and lower values over the oceans, similar to SAT.

3.3 Model – Observation Comparison: CSIRO Run 2

M-SSA analysis of section 3.1 suggests that the space-time patterns characterizing the observed SW are not reproduced in any of the CMIP5 model simulations we considered (see projection of the simulated climates onto the observed ST-EOFs in Fig. 4). What does this result based on automated identification of space–time patterns really mean? How exactly are the leading internal modes of CMIP5 models different from the observed SW? The three distinct possibilities in characterization of model-observation differences include the differences in the timescale, the differences in characteristic patterns and the differences in the sequence of patterns between the observed and model simulated internal modes. To address this question, we consider select simulations of the Commonwealth Scientific and Industrial Research Organization (CSIRO) Mk3 model. Barcikowska et al. (2017) showed that CSIRO control simulations reproduced realistic connections between the Atlantic and Pacific multidecadal variability similar to that in observations. Furthermore, Kravtsov et al. (2018) found the CSIRO model to have the

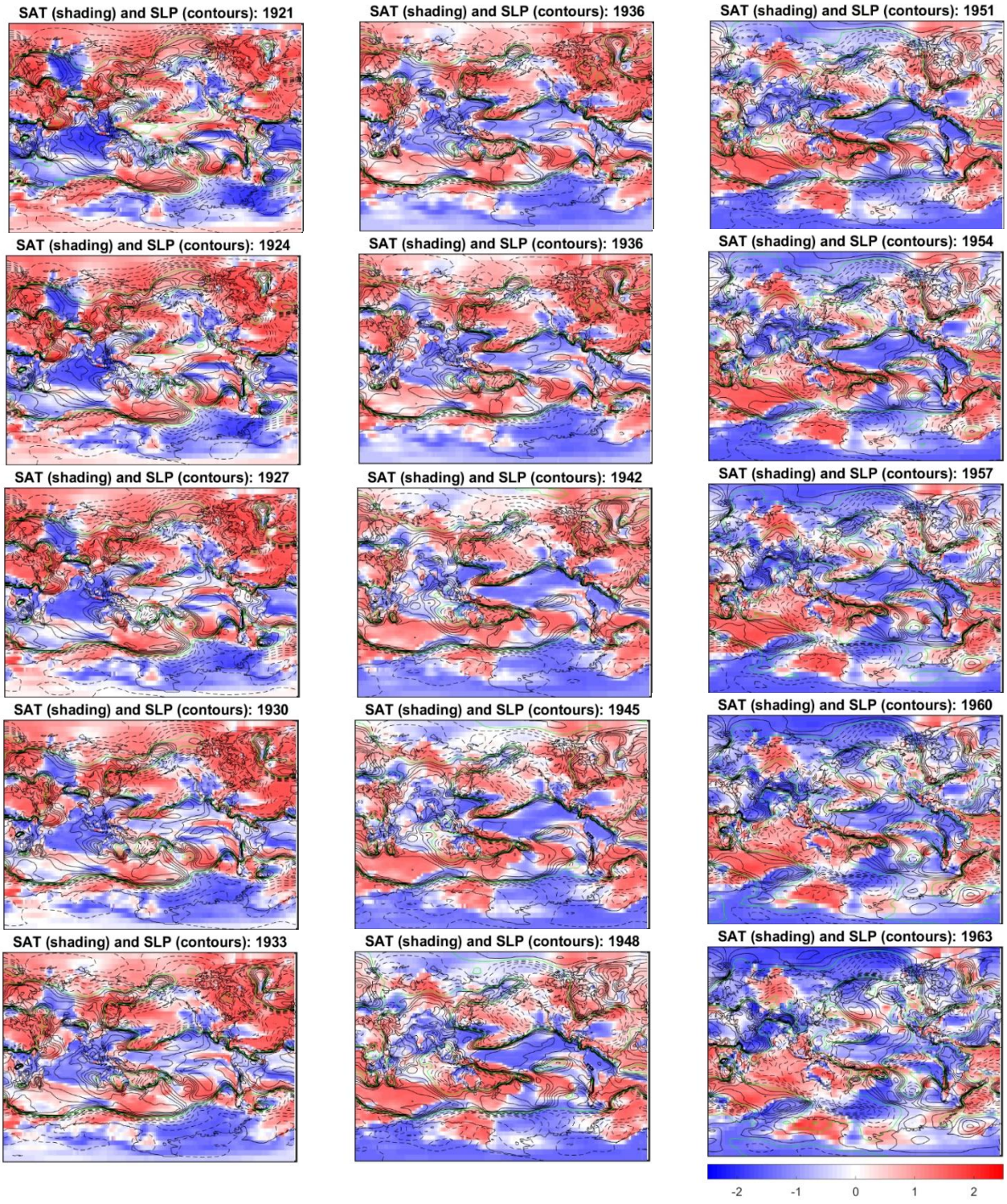

Figure 11: CSIRO Run 2 SAT/SLP RC SW: Simulated reconstructed SAT and SLP data from CSIRO run 2. Positive SLP data are denoted by solid black contours, negative by dashed contours, and 0 by green contours. Contours are spaced by 0.25. Stippling indicates statistically significant points. Positive values are warm colors and negative values are cool colors.

strongest “stadium wave” analogs in terms of the intensity of the leading M-SSA pair. Out of 10 available CSIRO simulations, we chose runs 2 and 9 since they are dominated by a multidecadal signal akin to the observed stadium wave in terms of the time scale. Run 3 exhibits similar connections between the Atlantic and Pacific variability and is briefly discussed later in Section 3.4.

Despite the similarity of the time scale, the SW structure of the CSIRO model defined by its leading M-SSA pair is different from the observed SW structure. Furthermore, since the CSIRO signal-to-noise ratio is higher than in observations, we smoothed CSIRO time series using 15-yr boxcar running-mean filter. To ensure a level playing field, we also repeated our M-SSA analysis for observations using 15-yr low-pass filtered data and obtained the stadium wave essentially identical to the one identified from unsmoothed, raw data (not shown).

Fig. 11 shows the CSIRO SW maps from run 2, analogous to the observed maps in Fig. 5. SAT and SLP spatial patterns found in models have structures that are more heterogeneous than in observations. Most of the North Atlantic and Arctic has anomalously warm temperatures, while most of the South Atlantic, Southern Ocean, and Indian Ocean have anomalously low temperatures. The Pacific has several small regions of positive and negative SAT anomalies. By 1930, an east-west SAT dipole forms in the Indian Ocean and North Pacific. Antarctica is predominately experiencing negative SAT anomalies, and the North Atlantic remains unchanged. While the spatial patterns remain fairly consistent, up through 1950 sees a weakening of the positive SAT anomalies in the Arctic and eventual transition to negative anomalies, strengthening of negative SAT anomalies in the equatorial Pacific, and strengthening of positive SAT anomalies in the South Atlantic and southwest Pacific extending down to the Southern Ocean. By 1963, the negative anomalies strengthen in the Arctic and weaken in the Antarctic,

positive phases weaken in the Atlantic, the South Pacific positive anomaly regions lessen, whereas most of the other smaller features remain relatively consistent.

SLP structures are not as diverse and exhibit negative anomalies in much of the polar regions, North Atlantic, and North Pacific. Positive Anomalies exist much throughout the Indian Ocean, South Pacific, and South Atlantic. These features remain relatively consistent until roughly 1950, where a strong dipole feature is established in the central North Pacific and North Atlantic. While negative SLP anomalies persist in the Antarctic region, positive anomalies begin to strengthen near Greenland. By 1963, smaller positive and negative anomalies appear in virtually all regional indices, removing the dipole structure in the North Pacific and Atlantic.

From the simulated SAT and spatial plots, smaller, more regional features emerge. These smaller features make it more difficult to identify a clear sequence of patterns. For example, when the Pacific contains several regions with positive and negative anomalies, the origin of a phase change is difficult to identify. These features sometimes coincide with features in the observed plot, however, since this is a simulated internal variability, they are expected to be different and any synchronization is accidental. For the SLP data, most of the regions do not contain structures that match observations. Since features in the SLP anomalies also become small and diverse, they often do not exhibit the broad features present in observation data where a sequence of patterns is obvious. For example, dipole features are present in the North and South Pacific in the simulated data, but they are often not in the same location as observations.

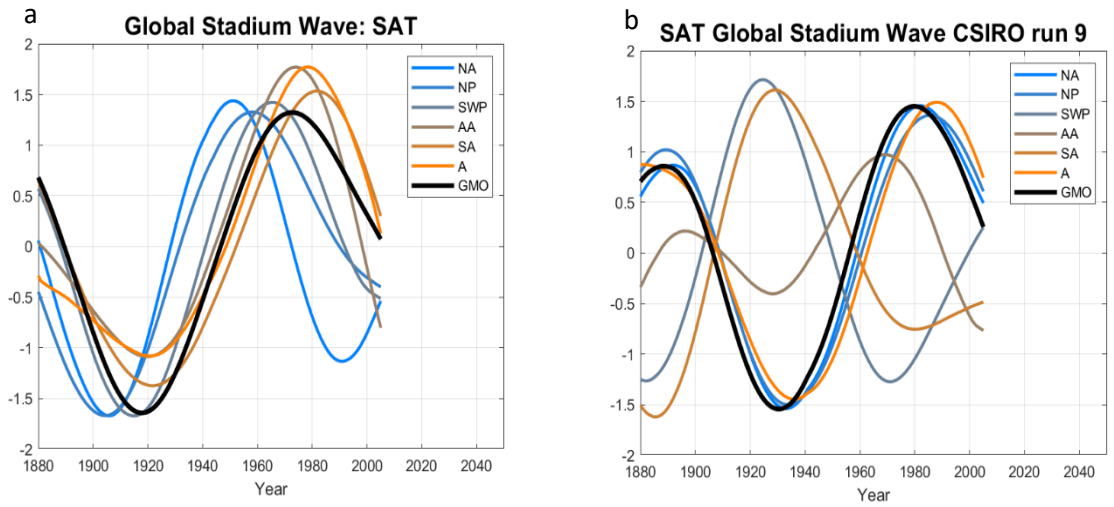

Figure 12: Regional Indices time series of observed RC SAT data for North Atlantic (NA), North Pacific (NP), southwest Pacific (SWP), Antarctic (AA), South Atlantic (SA), Arctic (A), and the global mean (GMO). ***(a)*** *observed RC SAT data* ***(b)*** *CSIRO run 2 RC SAT data*

Comparing the observed regional indices time series plot (**Fig. 12a**) to the simulated time series (**Fig. 12b**) helps determine the SAT timescale and sequence of patterns for the widely diverse spatial patterns in the 2D plots. First, an 80-year mode is present, similar to observations. Second, The Antarctic mode leads the North Pacific and Arctic modes, which are virtually synced, by ~30 years. This is different from observations, were the Arctic lags significantly behind the North Pacific and the observed variability originated in the North Atlantic. Lastly, the North Atlantic mode lags behind the North Pacific and Arctic by approximately 5 years, followed by the southwest Pacific and South Atlantic by approximately 30 years.

The magnitude of the stadium wave in the CSIRO run 2 for SAT and SLP is shown in Figs. 7 and 10 respectively. In Fig. 5, the magnitude of the stadium wave for CSIRO run 2 (yellow line) is smaller than observations. This indicates that less variance exists in all analyzed regions in CSIRO run 2. In Fig. 9, the magnitude of the stadium wave for CSIRO run 2 (yellow line) is smaller than observations in all regions except for the North Atlantic, where it is

Figure 13: CSIRO Run 9 SAT/SLP RC SW: Simulated reconstructed SAT and SLP data from CSIRO run 9. Positive SLP data are denoted by solid black contours, negative by dashed contours, and 0 by green contours. Contours are spaced by 0.25. Stippling indicates statistically significant points. Positive values are warm colors and negative values are cool colors.

comparable to observations. A key feature in this plot is the significant lack of variance in the Arctic compared to observations. This may indicate different dynamics present in this region in the model and not in observations. Noise in the internal variability would reduce the variability in the Arctic for CSIRO run 2, resulting in reduced magnitudes.

3.4 Model – Observation Comparison: CSIRO Run 9

The same analysis in the previous section was repeated for run 9 of the CSIRO model, including the spatial plot (**Fig. 13)**. Positive SAT regions include the South Atlantic, southern Indian Ocean, between 20 and 40°S for the western Pacific, and between 40 and 60°N for a portion of the North Pacific. A majority of other regions contain negative SAT anomalies. Structurally, these features are persistent through 1940 with the exception of the positive region in the North Pacific, which weakens to near-zero values and a small region in eastern Antarctica, which transitions to positive anomalies. The anomalies in all other regions, positive and negative, also appear to weaken. By 1950, positive SAT anomalies emerge in the tropical Pacific and North America. These regions degrade the larger structures present in the 1921 panel. Simultaneously, weaker positive regions and regions with near-zero values, like the extreme South Atlantic and Australian continent, exhibit a transition to a negative phase. By 1963, portions of the North Atlantic and Arctic transition to positive SAT anomalies.

Negative SLP Anomalies exist everywhere below 50°S (although weak), most of the Indian Ocean, and most of the South Atlantic. Positive anomalies exist over the entire Arctic, a majority of the southeast, tropical, and North Pacific, and a region along 40°S that stretches from the Cape of Good Hope to Australia. Up through 1940, most features remain intact, with the exception of the Arctic positive anomalies expanding south and a region in the South Atlantic converting to positive anomalies. Up through 1963, most of the spatial features remain, both in

relative shape and sign, except for the Arctic (becomes positive) and Indian Ocean (becomes negative).

SAT and SLP show that there is little agreement between CSIRO run 9 and observations. Features in this simulation are broader than in CSIRO run 2, covering roughly the same size areas as in observations (but not the same areas themselves), however the shape and phase are often in disagreement. Throughout a majority of the simulation, either the Arctic or Antarctic tend to be in opposite phase from observations.

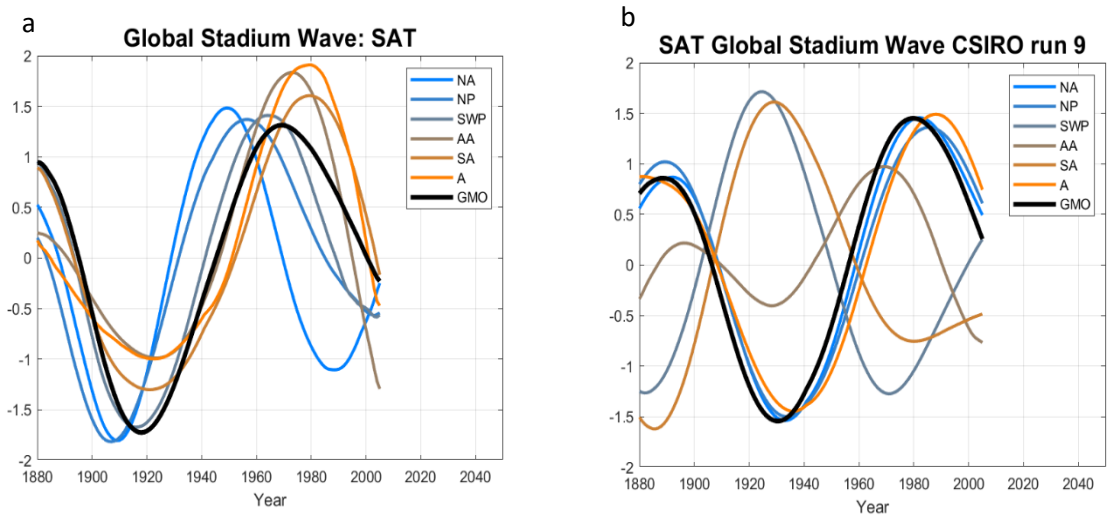

*Figure 14: Regional Indices time series of observed RC SAT data for North Atlantic (NA), North Pacific (NP), southwest Pacific (SWP), Antarctic (AA), South Atlantic (SA), Arctic (A), and the global mean (GMO). **(a)** observed RC SAT data **(b)** simulated RC SAT data from CSIRO run 9*

Regional indices plots show the timescale and sequence of pattern in CSIRO run 9 (**Fig. 14a**). Most indices have a timescale of ~90 years. This is slightly longer than those in observations (**Fig. 14b**). Four regions, and the global mean, experience two positive phases. The first has the Arctic before the North Pacific and the North Atlantic slightly trailing both, contrary to observations. Antarctica, although much weaker, is relatively in phase with the regions mentioned thus far. The southwest Pacific and South Atlantic occur approximately 60 years after

the former regions, with the South Atlantic slightly trailing the South Pacific. This is also not in observations. The second positive phase has the Antarctic signal first, followed by the North Atlantic, North Pacific, and Arctic. Lastly, the North Atlantic and Pacific, as well as the Arctic, are almost exactly phased in the model, which is not the case in observations.

Lastly, Figures 5 and 9 can once again be used to compare the magnitudes of different regions. With SAT data, CSIRO 9 magnitudes are lower for all regions except the Arctic, where variance is marginally higher. With SLP data, magnitudes are lower for all regions except in the Pacific. Since the Arctic and southwest Pacific is a relatively small region, overall variance is less globally in CSIRO 9 than observations.

We felt it was important to note that, once again, these two runs were chosen based off of the similar timescale of variability to observations. However, the sequence of events is often different. There are runs of CSIRO, such as run 3, that exhibits variability on a timescale of 40 years, but also contain a similar sequence of patterns. For example, the SW moves from the North Atlantic to the North Pacific. Barcikowska et al. (2017) analyzed this mode for this reason. Therefore, the selection of a particular model run is dependent on which features the observer wishes to isolate; the timescale at which the variability occurs (such as this study), the resulting spatial patterns, or the sequence of patterns (such as Barsikowska et al. 2017).

4. Discussion, Conclusions, and Future Work

This study found that the addition of SLP data not only replicates the same features when performing an SAT-only analysis but also allows for the analysis of the atmospheric component of the observed stadium wave.

By performing regional analysis, the high frequency variability present was partially filtered out and signal-to-noise ratio increased. This allowed for low-frequency signals to be isolated in the data and highlighted that simpler methods can be used to increase the signal-to-noise ratio. It also results in less variance being captured in the M-SSA plots, however most of the variance observed in the M-SSA modes are contained within the leading pair.

The leading pair was used to reconstruct the SAT and SLP data necessary to spatially and temporally observe the multidecadal features contained within the internal variability. The SAT plots showed that using combined PCA still generates the same spatial and temporal SAT patterns. More specifically, the observed SW from the SAT-only analysis is virtually identical to the one observed in the SAT/SLP analysis. SW magnitudes were also virtually the same, with the exception of the Arctic.

The SLP plots showed the atmospheric component of the global stadium wave and some key features. A dipole with striking similarity to the positive NAO phase was present in the North Atlantic. Another feature was observed in the North Pacific that resembled a North Pacific high — Aleutian Low dipole. With time, an Atlantic — Pacific gradient weakens, and a majority of the Pacific shifts to positive anomalies. The Arctic and North Pacific were the only two locations that showed anomalies with the same sign as SAT.

Several modes are present in these regions, all being characterized by distinctive spatial patterns and operating over a range of time scales, yet potentially influencing one another. We speculate that these modes and interactions between them contribute to generation and maintenance of the observed SAT/SLP SW in observations. For example, the SAT and SLP SW often exhibits opposite phases between the tropical Atlantic and eastern Pacific. Barcikowska et al. (2017), who performed M-SSA on linearly detrended and smoothed SAT, SLP, and surface wind observations and CMIP5 pre-industrial control run, showed similar features. They, among others (Li et al. 2016; McGregor et al. 2014) postulate that an "atmospheric bridge" exists between the Atlantic and Pacific oceans, more specifically between the tropical regions of these two basins. Warming in the tropical Atlantic SATs forces a displacement in SLP features, strengthening the Walker circulation and leading to cooling in the eastern Pacific. However, more analysis is needed to determine what processes are responsible for the above features.

Simulated data from CSIRO runs 2 and 9 were analyzed spatially and temporally to highlight their timescale, spatial patterns, and sequence of patterns to contrast them with observed features. These runs were chosen because they have a similar timescale of variability (~80-year mode). However, in both runs, spatial patterns and sequence of patterns were not similar to the observed SW. Most often, spatial patterns were smaller and had positive and negative anomalies contained within a small area, making it difficult to observe a sequence of events as well defined as the observed SW. When using the regional indices plots, it was apparent that the sequence of events was different. Regional variability did not show the SW originate in the North Atlantic, propagate to the North Pacific, etc.

In the future, it would be advantageous to analyze different models from the CMIP5 suite. The selection of model run is dependent on what analysis the observer wishes to perform.

With SAT-only observation, it was found that CSIRO had the highest amount of internal variability. This is not the case for combined SAT-SLP analysis, and it would be interesting to investigate how other runs from different models compare. Also, we based our decision to analyze these particular CSIRO runs because their variability has a similar timescale to observations. Pursuing runs with a similar sequence of patterns (such as Barcikowska et al. 2017), or perhaps spatial patterns, would be interesting. Also, a portion of the variance was removed from the common EOF analysis. Reintroducing this variance, by normalizing the SAT and SLP data in each model run by the standard deviation of the first PC of the ensemble mean of internal observations, rather than the standard deviation of the particular model run, is a potential fix to this problem. Lastly, and probably the most interesting future direction, would be to isolate and describe what teleconnections aid in the propagation of the stadium wave.

References

Barcikowska, M.J., T.R. Knutson, and R. Zhang, 2017: Observed and Simulated Fingerprints of Multidecadal Climate Variability and Their Contributions to Periods of Global SST Stagnation. *J. Climate*, **30**, 721–737, https://doi.org/10.1175/JCLI-D-16-0443.1

Cai, W., and coauthors, 2019: Pantropical Climate Interactions. *Science*, **363**, doi:10.1126/science.aav4236

Cassou, C., Y. Kushnir, E. Hawkins, A. Pirani, F. Kucharski, I. Kang, and N. Caltabiano, 2018: Decadal Climate Variability and Predictability: Challenges and Opportunities. *Bull. Amer. Meteor. Soc.*, 99, 479–490, https://doi.org/10.1175/BAMS-D-16-0286.1

Chylek, P., J.D. Klett, G. Lesins, M.K. Dubey, and N. Hengartner, 2014: The Atlantic Multidecadal Oscillation as a dominant factor of oceanic influence on climate, *Geophys. Res. Lett.*, **41**, 1689– 1697, doi:10.1002/2014GL059274

Compo, G. P. and Coauthors, (2011): The Twentieth Century Reanalysis Project. *Quart. J. Royal Meteorol. Soc*., **137**, 1–28, https://doi.org/10.1002/qj.776

Deser, C., and A. Phillips, 2017: An overview of decadal-scale sea surface temperature variability in the observational record. *Past Global Changes Mag.*, **25**, 2-6, doi: 10.22498/pages.25.1.2

d'Orgeville, M., and W.R. Peltier, 2007: On the Pacific Decadal Oscillation and the Atlantic Multidecadal Oscillation: Might they be related? *Geophys. Res. Lett.*, **34**, doi:10.1029/2007GL031584

Ghil, M., and coauthors, 2002: Advanced spectral methods for climatic time series, *Rev. Geophys.*, **40(1)**, 1003, doi:doi:10.1029/2000RG000092, 2002.

Hartmann, D.L., 2016: Matrix Methods: EOF, SVD, ETC. ATM 552 Notes, 42 pp, https://atmos.washington.edu/~dennis/552_Notes_4.pdf

England, M.H., and coauthors, 2014: Recent intensification of wind-driven circulation in the Pacific and the ongoing warming hiatus. *Nature Climate Change*, **4**, 222–227, https://doi.org/10.1038/nclimate2106

Kosaka, Y., and S Xie, 2013: Recent global-warming hiatus tied to equatorial Pacific surface cooling. *Nature*, **501**, 403–407 https://doi.org/10.1038/nature12534

Kravtsov, S., 2017: Pronounced differences between observed and CMIP5-simulated multidecadal climate variability in the twentieth century, *Geophys. Res. Lett.*, **44**, 5749–5757, doi:10.1002/2017GL074016.

Kravtsov, S. and C. Spannagle, 2008: Multidecadal Climate Variability in Observed and Modeled Surface Temperatures. *J. Climate*, **21**, 1104–1121, https://doi.org/10.1175/2007JCLI1874.1

Kravtsov, S., and D. Callicutt, 2017: On semi-empirical decomposition of multidecadal climate variability into forced and internally generated components. *Int. J. Climatol.*, **37**, 4417-4433, doi:10.1002/joc.5096

Kravtsov, S., C. Grimm, and S. Gu, 2018: Global-scale multidecadal variability missing in state-of-the-art climate models, *npj Climate Atmos. Sci*., 1-34, doi:10.1038/s41612-018-0044-6

Lewandowsky, S., J.S. Risbey, and N. Oreskes, 2016: The "Pause" in Global Warming: Turning a Routine Fluctuation into a Problem for Science. *Bull. Amer. Meteor. Soc.*, **97**, 723–733, https://doi.org/10.1175/BAMS-D-14-00106.1

Li, X., S. Xie, S. Gille, C. Yoo, 2016: Atlantic-induced pan-tropical climate change over the past three decades. *Nature Climate Change*, **6,** 275–279, https://doi.org/10.1038/nclimate2840

McGregor, S., A. Timmermann, M. Stuecker, M.H. England, M. Merrifield, F.-F. Jin and Y. Chikamoto, 2014: Recent Walker circulation strengthening and Pacific cooling amplified by Atlantic warming. *Nature Climate Change*, **4**, 888–892, https://doi.org/10.1038/nclimate2330

Meehl, G.A., and Coauthors, 2014: Decadal Climate Prediction: An Update from the Trenches. *Bull. Amer. Meteor. Soc.*, **95**, 243–267, https://doi.org/10.1175/BAMS-D-12-00241.1

Mestas-Nuñez, A.M., and A.J. Miller, 2006: Interdecadal variability and climate change in the eastern tropical Pacific: A review. *Prog. Oceanogr.*, **69**, 267-284, https://doi.org/10.1016/j.pocean.2006.03.011

Taylor, K.E., R.J. Stouffer, and G.A. Meehl, 2012: An Overview of CMIP5 and the Experiment Design. *Bull. Amer. Meteor*. Soc., 93, 485–498, https://doi.org/10.1175/BAMS-D-11-00094.1

Wilks, D.S., 2011: Principle Component (EOF) Analysis. *Statistical Methods in the Atmospheric Sciences*, Acad. Press, 519-562

Wyatt, M.G., S. Kravtsov, and A.A. Tsonis, 2012: Atlantic Multidecadal Oscillation and Northern Hemisphere's climate variability. *Climate Dyn*. **38**, 929–949, https://doi.org/10.1007/s00382-011-1071-8

Yeager, S.G., and J.I. Robson, 2017: Recent Progress in Understanding and Predicting Atlantic Decadal Climate Variability. *Curr. Clim. Change Rep.*, **3**, 112–127, https://doi.org/10.1007/s40641-017-0064-z

Zhang, R., R. Sutton, G. Danabasoglu, Y.-O. Kwon, R. Marsh, S.G. Yeager, D. E. Amrhein, C. M. Little, 2019: A review of the role of the Atlantic Meridional Overturning Circulation in Atlantic Multidecadal Variability and associated climate impacts. *Rev. Geophys.*, **57**, 316– 375. https://doi.org/10.1029/2019RG000644